

Single Crystal Microwires of *p*-DTS(FBTTh₂)₂ and Their Use in the Fabrication of Field-Effect Transistors and Photodetectors

QiuHong Cui,* Yuanyuan Hu, Cheng Zhou, Feng Teng, Jianfei Huang, Andriy Zhugayevych,* Sergei Tretiak, Thuc-Quyen Nguyen, and Guillermo C. Bazan*

Single crystal microwires of a well-studied organic semiconductor used in organic solar cells, namely *p*-DTS(FBTTh₂)₂, are prepared via a self-assembly method in solution. The high level of intermolecular organization in the single crystals facilitates migration of charges, relative to solution-processed films, and provides insight into the intrinsic charge transport properties of *p*-DTS(FBTTh₂)₂. Field-effect transistors based on the microwires can achieve hole mobilities on the order of $\approx 1.8 \text{ cm}^2 \text{ V}^{-1} \text{ s}^{-1}$. Furthermore, these microwires show photoresponsive electrical characteristics and can act as photoswitches, with switch ratios over 1000. These experimental results are interpreted using theoretical simulations using an atomistic density functional theory approach. Based on the lattice organization, intermolecular couplings and reorganization energies are calculated, and hole mobilities for comparison with experimental measurements are further estimated. These results demonstrate a unique example of the optoelectronic applications of *p*-DTS(FBTTh₂)₂ microwires.

well-established strategy to achieve high-performance donor materials relevant to the fabrication of organic solar cells is to link electron rich (donor, D) and electronegative (acceptor, A) structural units in conjugation with each other.^[7,8] The resulting chromophores exhibit intramolecular charge transfer characteristics and thus optical transitions suitable for light harvesting. Relative to their polymeric counterparts, molecular systems offer well-defined chemical structures, which provide absence of batch-to-batch variations.^[9] Moreover, molecular systems can in principle provide single crystals suitable for X-ray characterization and therefore provide a platform to evaluate relationships between intermolecular organizations and optoelectronic properties in the solid state.

The compound *p*-DTS(FBTTh₂)₂ (*7,7'*-(4,4-bis(2-ethylhexyl)-4H-silolo[3,2-b:4,5-b']dithiophene-2,6-diyl)bis(6-fluoro-4-(5'-hexyl-[2,2'-bithiophen]-5-yl)benzo[c]-[1,2,5]thiadiazole, see Figure 1a) has been used to study the properties of molecular photovoltaic devices.^[10–12] Various bulk heterojunction (BHJ) solar cells based on blends comprised of *p*-DTS(FBTTh₂)₂ with fullerene^[13] or nonfullerene acceptors^[14,15] have been constructed and exhibit excellent photovoltaic performance. Several processing techniques have

1. Introduction

Solution-processed organic semiconductors are a relevant topic of research because of their potential applications in modern electronics.^[1–3] Rational design strategies at the molecular level have emerged to tailor molecular orbital energy levels and optical gaps with the goal of improving device performance.^[4–6] For example, in the field of solar cells, one effective and

Dr. Q. Cui, Prof. F. Teng
Key Laboratory of Luminescence and Optical Information
Ministry of Education
School of Science
Beijing JiaoTong University
Beijing 100044, China
E-mail: qhcui@bjtu.edu.cn

Dr. Y. Hu, Dr. C. Zhou, J. Huang, Dr. S. Tretiak
Prof. T.-Q. Nguyen, Prof. G. C. Bazan
Center for Polymers and Organic Solids
Departments of Chemistry & Biochemistry and Materials
University of California
Santa Barbara, CA 93106, USA
E-mail: bazan@chem.ucsb.edu

Dr. Y. Hu
School of Physics and Electronics
Hunan University
Changsha 410082, China

Prof. A. Zhugayevych, Dr. S. Tretiak
Skolkovo Institute of Science and Technology
Moscow 143026, Russia
E-mail: a.zhugayevych@skoltech.ru

Dr. S. Tretiak
Theoretical Division
Los Alamos National Laboratory
Los Alamos, NM 87545, USA

 The ORCID identification number(s) for the author(s) of this article can be found under <https://doi.org/10.1002/adfm.201702073>.

DOI: 10.1002/adfm.201702073

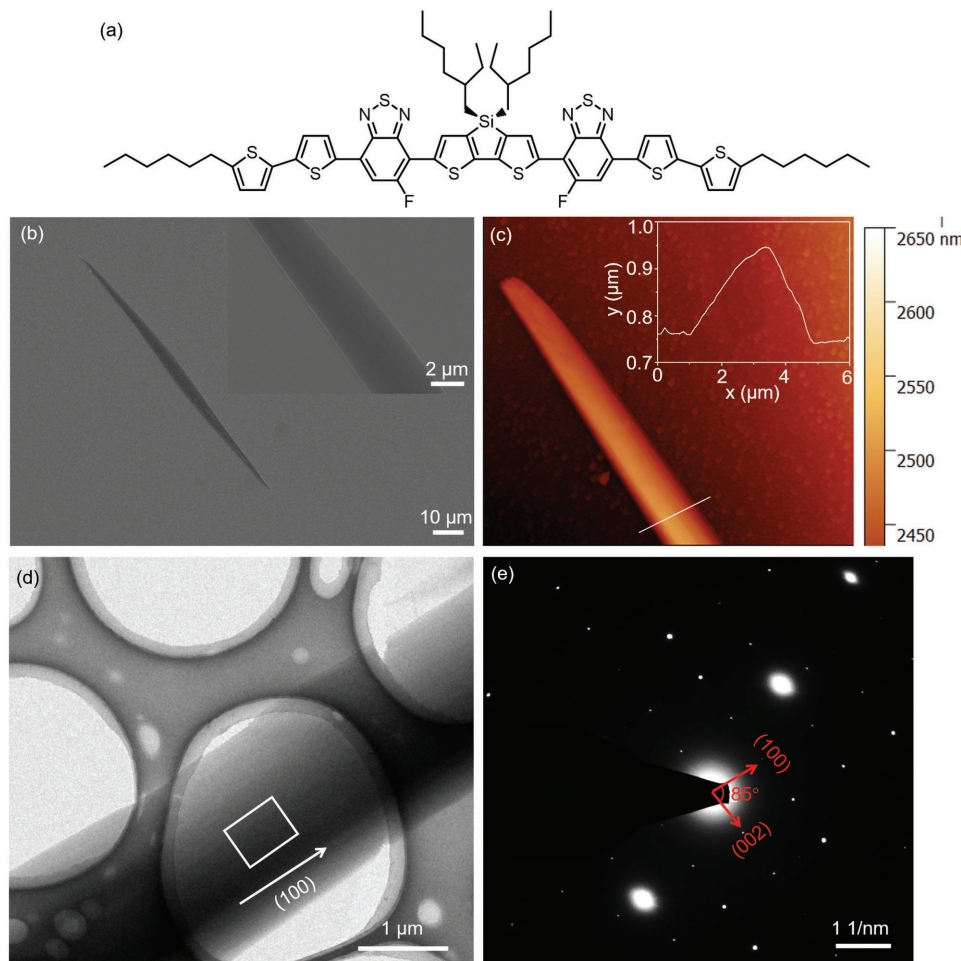


Figure 1. a) Molecular structure of *p*-DTS(FBTTh₂)₂. b) SEM image of the *p*-DTS(FBTTh₂)₂ microwire. Inset: high magnification the SEM image. c) AFM image of a single *p*-DTS(FBTTh₂)₂ microwire. Inset: the corresponding cross-sectional profile from the white line. d) TEM image of a single wire. e) SAED pattern collected from the microarea marked with a white square.

been developed in order to optimize the power conversion efficiency.^[16] For example, solvent additives have been used to modify the nanoscale morphology of the BHJ layer by altering the morphological length scales of the donor and acceptor phases.^[17–19] Moreover, high-molecular-weight insulating polymers were added in the blends systems to control the thickness of the active layer.^[20,21]

The intrinsic charge transport in *p*-DTS(FBTTh₂)₂ is a key parameter to understand any device that relies on its optoelectronic properties. Obtaining this information is challenging in BHJ layers, because of structural and compositional complexity, and even when examining neat films because of the formation of polycrystalline morphologies in which charge carrier transport is limited by the presence of grain boundaries. Hence, using single-crystals of *p*-DTS(FBTTh₂)₂ not only provides promising possibilities for fabricating high-quality devices, but also provides a platform to understand transport in highly ordered systems. In this contribution, we describe the preparation of quasi 1D *p*-DTS(FBTTh₂)₂ single crystals, which exhibit hole mobilities of $\approx 1.8 \text{ cm}^2 \text{ V}^{-1} \text{ s}^{-1}$ and comprise highly sensitive photodetectors with a switching ratio of ≈ 1000 . Our theoretical density functional theory (DFT) modeling demonstrates

an efficient charge transport along the nanowire owing to significant intermolecular couplings and charge hopping distances in π -stacks with calculated hole mobilities being in line with experimental observations. This work provides a valuable reference for developing novel optoelectronic devices based on *p*-DTS(FBTTh₂)₂, and for exploring innovative new applications.

2. Results and Discussion

The chemical structure of *p*-DTS(FBTTh₂)₂ (Figure 1a) provides a planar electronically delocalized framework that facilitates π - π interactions between molecules and tight intermolecular packing; features beneficial for obtaining self-assembled microstructures.^[22–26] Figure 1b provides a typical scanning electron microscopy (SEM) image of a *p*-DTS(FBTTh₂)₂ microwire obtained via the solution-phase self-assembly process, see the Experimental Section for preparation details. One observes a largely defect-free structure with smooth surfaces. The typical height ($\approx 200 \text{ nm}$) and width ($\approx 2 \mu\text{m}$) of the wire, together with the shape of the cross section, are illustrated in the atomic force microscopy (AFM) image provided in Figure 1c. The cross-polarized optical

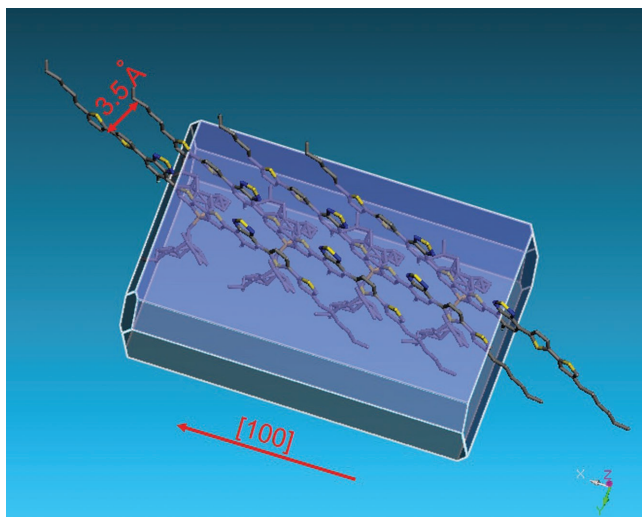


Figure 2. Estimate of the crystal growth direction of *p*-DTS(FBTTh₂)₂ microwires based on Bravais–Friedel–Donnay–Harker (BFDH) law using Materials Studio package. It can be seen that the *p*-DTS(FBTTh₂)₂ microwire has a close packed 1D π -stacking of the molecules along the [100] direction (i.e., the a axis). Here is the x axis.

microscopy images of the *p*-DTS(FBTTh₂)₂ microwire (Figure S1, Supporting Information) confirm the single crystalline nature of the fabricated wires. The transmission electron microscopy (TEM) image and selected area electron diffraction (SAED) pattern in Figure 1d,e indicate that the crystals grow preferentially along the [100] direction. This is further confirmed by the X-ray diffraction (XRD) pattern of *p*-DTS(FBTTh₂)₂ microwires (Figure S2, Supporting Information), which in the case of the microwires shows the dominance of (100) lattice planes.

The organization of *p*-DTS(FBTTh₂)₂ reveals 1D π -stacking of the molecules along the a axis (Figure 2). These observations are consistent with previous estimates of intermolecular energetics showing that the intrastack binding energy is 5 times larger than the interstack interaction energy.^[6] The intermolecular distance along the stacking direction is as short as 3.5 Å, which results in good overlap between adjacent π orbitals and should facilitate migration of charges.^[19] The slip-stack geometry ensures extra benefits for transport since each hop of a charge carrier along the π -stack results in a large displacement of the center of charge distribution, 9.3 Å.

UV-visible absorption spectroscopy was used to probe the optical properties of *p*-DTS(FBTTh₂)₂ in solution, as cast films, and in the form of microwires, see Figure 3. As previously reported, both the absorption maximum (λ_{max}) and onset (λ_{onset}) have a bathochromic shift in going from solution to the solid. The λ_{max} red shift is 88 nm (from 590 to 678 nm); and the λ_{onset} red shift is 130 nm (from 670 to 800 nm). Compared to the film, the absorption of the microwires shows a more pronounced aggregation peak at 691 nm, with a further bathochromic shift. These phenomena suggest the presence of a larger fraction of ordered content, consistent with the single crystal characteristics.

Field-effect transistors (FETs) were used to investigate electrical properties and were constructed by dropping microwires atop a SiO₂ substrate containing Au bottom electrodes

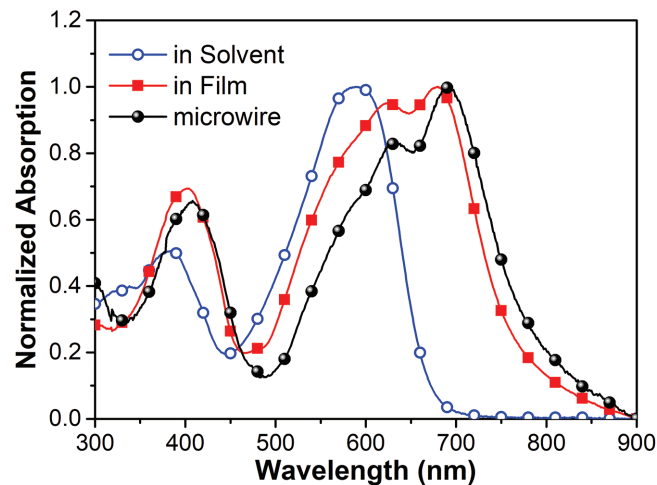


Figure 3. Normalized UV-visible absorption spectra of the *p*-DTS(FBTTh₂)₂ in solution (chlorobenzene), thin film and microwires.

(Figure 4a). The resulting device output and transfer characteristics, shown in Figure 4b,c, reveal excellent p-channel transport behavior. The transfer curves in the saturation regime show almost ideal transistor characteristic, i.e., the sqrt current versus gate voltage curves demonstrate linear fits (see Figure S3 in the Supporting Information). In addition, negligible hysteresis was observed, which indicates that there are few traps at the dielectric/semiconductor interface. The hole mobility μ_h was calculated from the saturation regime using equation

$$I_d = \mu_h W C_i (V_g - V_{th})^2 / 2L \quad (1)$$

in which C_i is the gate dielectric capacitance per unit area, L is the channel length, and W is the width of the *p*-DTS(FBTTh₂)₂ microwire bridging the source and drain electrodes as obtained by using an optical microscope.

The maximum field-effect mobility (μ_{max}) of the *p*-DTS(FBTTh₂)₂ microwire FETs was estimated to be $\approx 1.8 \text{ cm}^2 \text{ V}^{-1} \text{ s}^{-1}$ and the average of the mobilities (μ_{ave}) was $1.6 \pm 0.19 \text{ cm}^2 \text{ V}^{-1} \text{ s}^{-1}$. It is worth mentioning that this mobility is calculated without removing the effect of contact resistance. In fact, as seen in the output curves, the contact resistance plays a significant role in FET current profiles, thus the mobilities reported represent a lower limit.

Hole mobilities of films were also measured for comparison. The device was fabricated by spin coating a *p*-DTS(FBTTh₂)₂ solution in chlorobenzene on octadecyltrichlorosilane (ODTS)-passivated SiO₂ substrates with Au bottom-contact electrode, followed by annealing at 100 °C for 10 mins. The AFM image exhibits the morphology of annealed films in Figure 4d, which shows the typical microcrystalline nature of small-molecule films. Typical output and transfer characteristics of FETs based on *p*-DTS(FBTTh₂)₂ film are provided in Figure 4e,f. The μ_{max} of the *p*-DTS(FBTTh₂)₂ film was calculated to be $0.09 \text{ cm}^2 \text{ V}^{-1} \text{ s}^{-1}$ and the μ_{ave} was $0.08 \pm 0.01 \text{ cm}^2 \text{ V}^{-1} \text{ s}^{-1}$. The field-effect mobilities observed with the microwires are therefore ≈ 20 times larger than that observed in the films, supporting the high quality of the microwire crystals and the more efficient charge transport along the lattice.

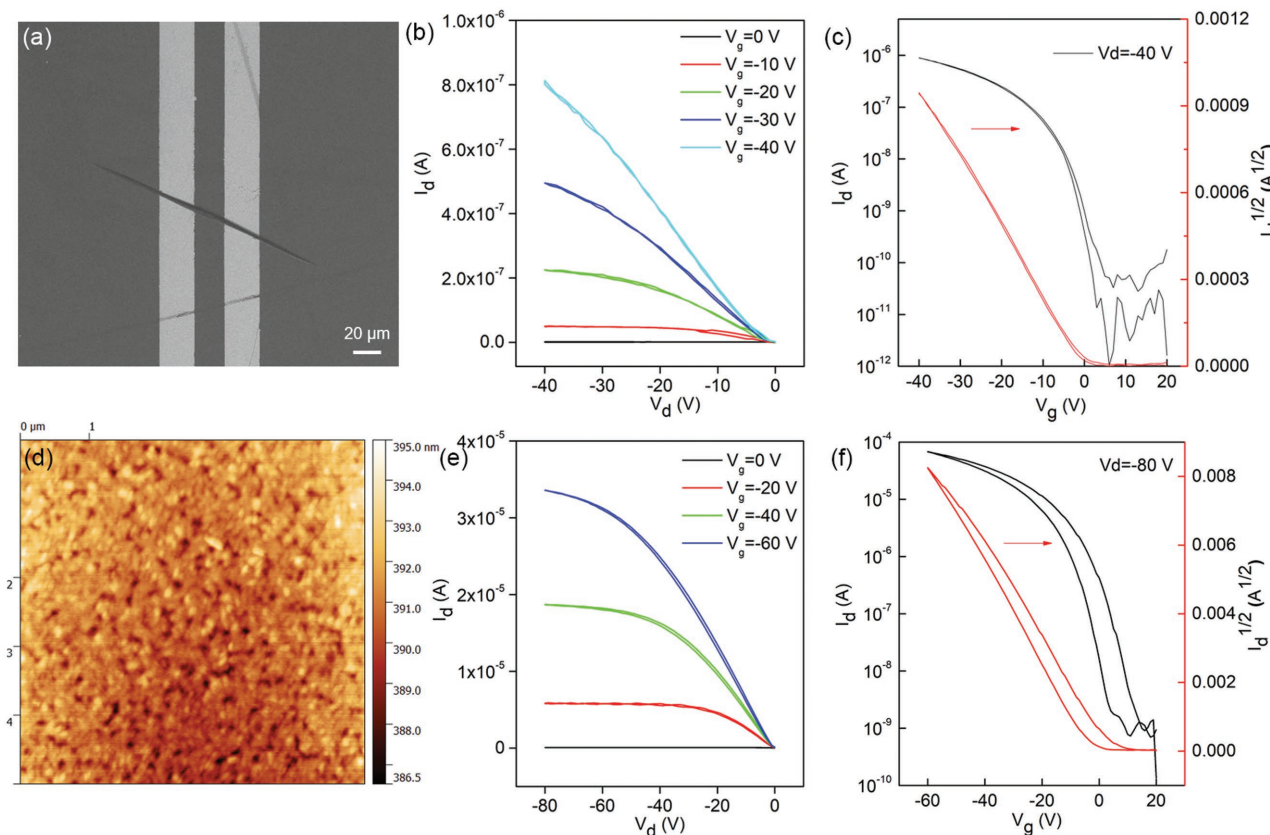


Figure 4. a) SEM image of the device with an individual microwire. b) Output and c) transfer characteristics (channel length, $L = 20 \mu\text{m}$, channel width, $W = \approx 3 \mu\text{m}$, which is the width of the microwire) of the device. d) AFM of the p -DTS(FBTTh_2) $_2$ film. e) Output and f) transfer characteristics (channel length, $L = 20 \mu\text{m}$, channel width, $W = 1000 \mu\text{m}$) of the film device.

Theoretical calculations of charge carrier transport confirm that p -DTS(FBTTh_2) $_2$ is an excellent hole transporter along the [100] crystallographic direction. Due to a combined effect of large intermolecular coupling, 100 meV and a large hopping distance, 9 Å, the estimated room-temperature mobility is on the order of $10 \text{ cm}^2 \text{ V}^{-1} \text{ s}^{-1}$ (within the small Holstein polaron hopping approximation, see the Supporting Information for detailed description of theoretical modeling). The transport is highly anisotropic with 2–3 orders of magnitude lower mobility along other directions. Although not accessible experimentally at this point, it is worth pointing out that the electron mobility is one order of magnitude smaller because of smaller intermolecular coupling, 15 meV. This is caused by localization of the lowest unoccupied molecular orbital on the electron-accepting unit (i.e., fluorinated benzothiadiazole fragment) within a single chromophore, which reduces the electron wave-function overlap for slip-stack geometries of a crystal, thus decreasing the net intermolecular interaction.

Though the difference between the calculated and measured values of the mobility is within the accuracy of modern methods,^[27] there are several important factors affecting calculated and measured mobilities. First of all, we lack perfect registry between the orientation in the crystal relative to the perfectly aligned π – π stack previously determined in the single crystal determination, as assumed in our modeling. The calculated mobility is for an ideal crystal and thus the experimental

value will be lower because of intrinsic intramolecular and intermolecular disorder and finite-size effects present in a realistic material. Effects of disorder are especially pronounced for quasi 1D transport, which is the case for holes in a p -DTS(FBTTh_2) $_2$ crystal. This crystal has intrinsic conformational disorder of side chains and terminal thiophene rings.^[6] While the direct effect of each of such geometric distortions on hole energy is small (e.g., <5 meV for flipping terminal ring), the cumulative effect including ensuing distortions of intermolecular couplings may be substantial. On surface and grain boundaries conformational disorder is expected to be more pronounced because of the flexibility of p -DTS(FBTTh_2) $_2$ molecule.^[6] Importantly, the conformer observed in the crystal is not the lowest energy conformer of the molecule itself. In such case relaxed geometries usually trap charge carriers. In particular, flipping one central dihedral stabilizes the highest occupied molecular orbital by 15 meV. Intermolecular disorder influences mainly electronic couplings, so that average squared couplings should be used as a rough approximation.^[27] Therefore, a systematic error is expected if the squared coupling reaches an extremum at the equilibrium geometry. This is the case of p -DTS(FBTTh_2) $_2$ crystal: the intrastack hole coupling is near its maximum and thus a disorder-averaged value can be substantially smaller. All the discussed effects combined decrease the above estimate of $10 \text{ cm}^2 \text{ V}^{-1} \text{ s}^{-1}$ toward the experimentally measured value. Finally, the absence of Ohmic contacts observed in Figure 2b

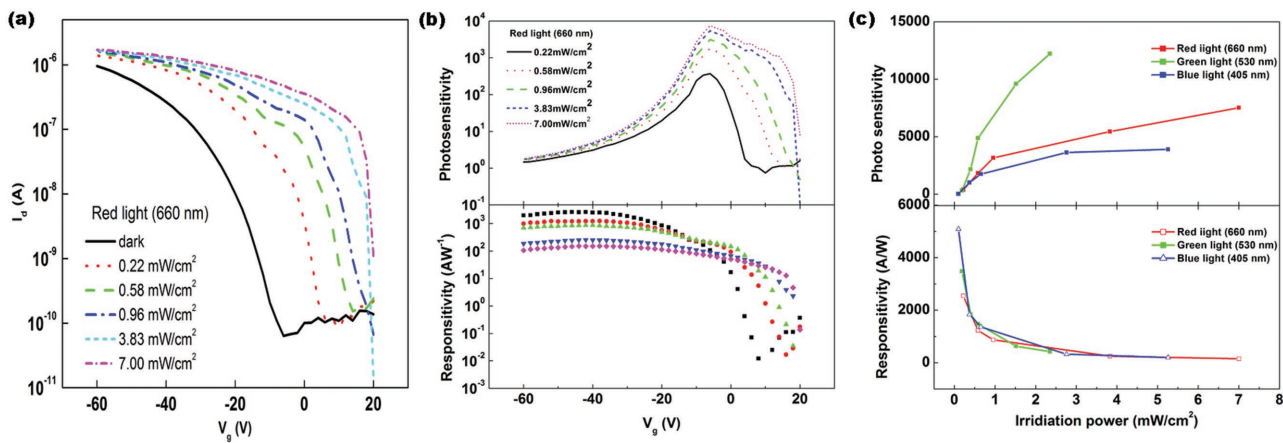


Figure 5. a) The transfer curves of the devices when irradiated by red light (660 nm) with different intensity. b) The dependence of photosensitivity and responsitivity on gate voltage, which were extracted from (a). c) The dependence of photosensitivity ($V_g = -6$ V) and responsitivity ($V_g = -40$ V) on irradiation power for three lights.

further leads to a decrease in the mobility determined from the transfer characteristics.

Because of the broad optical absorption shown in Figure 3, it is reasonable to expect that substantial numbers of charge carriers will be generated upon excitation by light at 660 nm.^[28–30] Combined with the fact that charge transport in the crystals is efficient, *p*-DTS(FBTTh₂)₂ microwire crystals have the potential to be especially suitable for fabricating phototransistors. The results of these studies are summarized in Figure 5. Figure 5a displays transfer characteristics of the microwire device measured in the dark and under illumination with different power. Based on the transfer curves shown in Figure 5a, the photosensitivity (P) and responsivity (R) are calculated by following equation

$$P = \frac{I_{\text{light}} - I_{\text{dark}}}{I_{\text{dark}}} \quad (2)$$

$$R = (I_{\text{light}} - I_{\text{dark}})/P_{\text{irradiation}} \quad (3)$$

where I_{dark} and I_{light} are the I_{ds} measured in dark and under illumination, respectively, and $P_{\text{irradiation}}$ is the power of the irradiation light. Figure 5b compares the P and R of *p*-DTS(FBTTh₂)₂ microwire devices as a function of V_g . It is seen that the P of the device is between 10^3 and 10^4 , and that R can be as high as 3×10^3 A W⁻¹, which are excellent values for a single-component organic phototransistor.^[31–35] We also compared the photoresponse to light of different wavelengths. As seen in Figure 5c, when green light or blue light is used as the light source, either the P or R can be further improved, depending on the irradiation power (see additional data in the Supporting Information). Altogether, these results demonstrate that *p*-DTS(FBTTh₂)₂ microwire crystals exhibit promising properties for applications in photodetectors.

We also compared the performance of phototransistor devices made from *p*-DTS(FBTTh₂)₂ microwires and films (Figure 6a,b). One observes that the maximum P (P_{max}) of the microwire transistor is two orders larger than that of the film

device (Figure 6c). This increase likely reflects the lower density of traps and absence of grain boundaries, which results in more efficient transport of photo-generated charge carriers.

In addition, the time-dependent photoresponses of the two devices were measured by periodically turning on and off the light at a constant applied voltage of $V_g = 10$ V and $V_{\text{ds}} = -80$ V. Figure 6d illustrates how the current across the microwire device under illumination increases substantially relative to the dark conditions. These “on”–“off” processes can be repeated multiple times. The “on”-state and “off”-state currents for each of the three cycles indicate reversible and stable characteristics with switching ratio of around 1000. The rising time (τ_r) and decay time (τ_d) were determined by an exponential decay equation,^[36] which are 2.5 and 2.2 s, respectively. In comparison, the current of the film device increases during the light on process, suggesting electron trapping in the film, which can induce further hole injection. The rising time is thus quite large, with $\tau_r > 9$ s. In the off process, the dark current is still quite high and decreases with time ($\tau_d = 1.8$ s), implying trapping of holes in the device. Thus, the on/off switch ratio for this device is much lower than the microwire device as a result of a higher density of traps. The high quality of the microwire crystal not only improves photosensitivity, but also reduces the density of traps, resulting in stable device performance.

3. Conclusion

Crystalline microwires of *p*-DTS(FBTTh₂)₂ can be readily prepared via solution-phase self-assembly. TEM images of individual microwires and their corresponding SAED patterns indicate that each microwire is a single crystal. Such wires can serve as the semiconductor element in the fabrication of field-effect transistors. These devices demonstrate excellent p-transport behavior, with measured hole mobilities on the order of ≈ 1.8 cm² V⁻¹ s⁻¹, which match theoretical estimates when considering internal lattice disorder and contact resistance in the devices. Moreover, phototransistors based on these microwire crystals were fabricated and their performance as

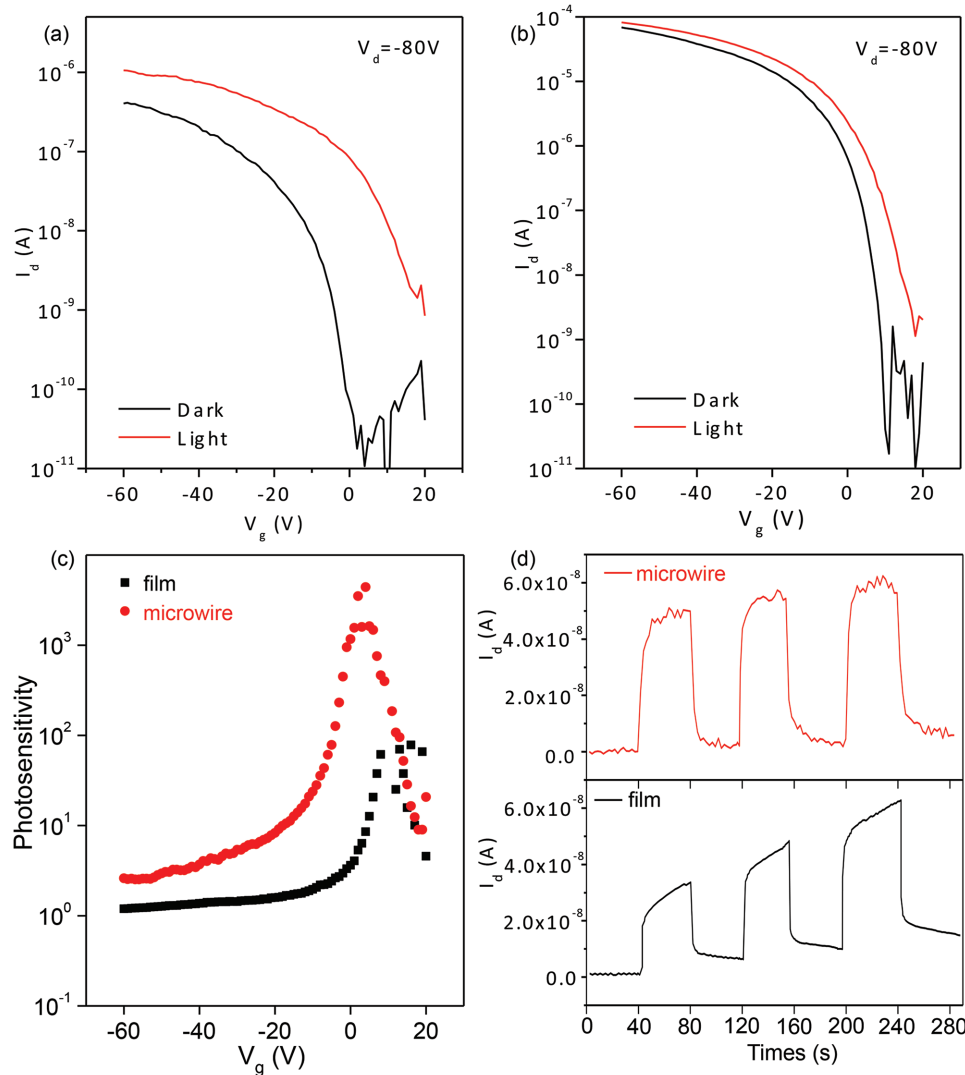


Figure 6. Transfer ($V_d = -80$ V) characteristics of the a) microwire device and b) film device when measured in dark and under illumination (660 nm, 5 mW cm $^{-2}$). c) Photosensitivity of *p*-DTS(FBTTh $_2$) $_2$ microwire and film device versus the gate bias calculated based on dark and illuminated transfer curves. d) Photoswitching (at bias $V_g = 10$ V and $V_d = -80$ V) characteristics of the wire and film devices.

photodetectors was investigated. High photosensitivity of 10^4 – 10^5 and responsitivity of about 5000 A W $^{-1}$ were observed. Indeed, reversible photoswitches based on individual microwires can be fabricated with a switch ratio over 1000 . In particular, the performance of the phototransistors based on these microwire crystals was found to be substantially improved relative to what is observed using *p*-DTS(FBTTh $_2$) $_2$ films. The results demonstrated in this work provide a useful baseline measure for the design and synthesis of high quality optoelectronic elements based on the general class of materials exemplified by *p*-DTS(FBTTh $_2$) $_2$, in particular for miniaturized devices.

4. Experimental Section

Preparation of *p*-DTS(FBTTh $_2$) $_2$ Microwires: A simple solution-phase self-assembly procedure was used that involves application of

different solvents and a slow decrease in temperature.^[37] Specifically, $100\ \mu\text{L}$ of *p*-DTS(FBTTh $_2$) $_2$ chlorobenzene solution ($2\ \text{mg mL}^{-1}$, good solvent) was rapidly injected into $2\ \text{mL}$ of hexane as the poor solvent at $60\ ^\circ\text{C}$. At this temperature hexane can dissolve *p*-DTS(FBTTh $_2$) $_2$, resulting in a homogeneous distribution of molecules. Upon cooling at a speed of $\approx 1\ ^\circ\text{C min}^{-1}$, the solubility of *p*-DTS(FBTTh $_2$) $_2$ decreases, inducing the controlled precipitation and crystallization assisted via π – π interactions. It is worth noting that increasing the concentration of the *p*-DTS(FBTTh $_2$) $_2$ chlorobenzene solution results in poor quality and distribution of the crystals. Other preparation conditions were tested that led to less successful microwires formation, including different solvents (good solvents: trichloromethane; poor solvents: water, ethanol, or methanol) and different temperatures (such as 40 or $80\ ^\circ\text{C}$).

Fabrication of FET Devices: Charge transport measurements utilized FETs prepared using bottom-gate, bottom-contact structures. Highly doped silicon wafers (0.001 – $0.005\ \Omega\ \text{cm}^{-1}$) with $300\ \text{nm}$ of thermally grown SiO $_2$ were used as the substrate. Standard lithography procedures were used to pattern the wafers with $50\ \text{nm}$ gold electrodes using $5\ \text{nm}$ of nickel as an adhesion layer. The *p*-DTS(FBTTh $_2$) $_2$ solutions at

15 mg mL⁻¹ in chlorobenzene were then spin-coated on substrates to fabricate the film FET devices. The microwire devices were constructed by directly dropping the suspension solution of fabricated *p*-DTS(FBTTh₂)₂ microwires atop the bottom-contact substrates.

Characterization: Microwires of *p*-DTS(FBTTh₂)₂ were initially examined by SEM (Hitachi S-4800). TEM and SAED were carried out using a JEOL 2010. AFM images were collected in air under ambient conditions on multiple sets of films using the Innova scanning probe microscope (Veeco). Silicon probes with spring constants of 40 N m⁻¹ and resonant frequencies of 300 KHz (Budget Sensors) were used for tapping mode AFM measurements. UV-Vis absorption spectra were recorded on a Shimadzu UV-2401 PC dual beam spectrometer and Perkin Elmer Lambda 750 UV/Vis spectrometer. The current-voltage (*I*-*V*) characteristics of OFETs and photoresponse characteristics were recorded in a nitrogen glove box with a Keithley 4200 semiconductor characterization system.

Computational Methodology: Our theoretical approach is based on DFT calculations performed with Gaussian 09 program.^[38] CAM-B3LYP density functional^[39] is used combined with 6-31G* basis set. Among methods of the same computational complexity, this pair has been shown to provide reliable results for large π -conjugated molecules.^[6,40] Electrostatic effects of a solvent are modeled by CPCM (conductor-like polarizable continuum model).^[41] Vibronic couplings are calculated in three steps: (1) initial estimate is made for the planarized hydrogen-passivated π -conjugated backbone of a molecule by projecting atomic displacements between two states onto vibrational modes; (2) obtained couplings are then rescaled to match the polaron relaxation energy obtained via energy differences as described in the Supporting Information; (3) finally, fully classical modes are added (formally with zero frequency but nonzero contribution to polaron relaxation energy) to compensate the difference in relaxation energy between the molecule and its backbone. The calculated vibronic couplings for excitons are then used to construct vibrationally resolved UV-Vis absorption band and compare it with experiment (Supporting Information). Intermolecular couplings for electrons and holes between a pair of molecules (dimer) are calculated by block diagonalization of the electronic Hamiltonian derived from the Fock matrices of the dimer and its constituents.^[27] Intermolecular couplings for excitons are calculated by a variant of Mulliken-Hush methods detailed in ref. [42]. Charge carrier and exciton transport was modeled using the Holstein Hamiltonian whose parameters are estimated from DFT calculations as described above. The Hamiltonian is solved in the small polaron hopping approximation to estimate charge carrier mobility and exciton diffusion length.^[27] The validity of this approximation is verified by estimating polaron band narrowing factor in the Supporting Information. The uncertainty in calculation of spectral overlap and its temperature dependence are also investigated in the Supporting Information.

Supporting Information

Supporting Information is available from the Wiley Online Library or from the author.

Acknowledgements

Work at UCSB was funded through the National Science Foundation under grant DMR 1411240. This work was also financially supported by the China Postdoctoral Science Foundation (Grant Nos. 2015M570924 and 2016T90030) and the National Natural Science Foundation of China (Grant No. 51603010). A.Z. acknowledges financial support by Volkswagen foundation (A115678 ref. 90486). This work was performed in part at the Center for Integrated Nanotechnologies (CINT), a U.S. Department of Energy, and the Office of Basic Energy Sciences user facility, at Los Alamos National Laboratory (LANL).

Conflict of Interest

The authors declare no conflict of interest.

Keywords

charge carrier mobility, field-effect transistors, organic semiconductors, photodetectors, single-crystals

Received: April 19, 2017

Revised: September 28, 2017

Published online:

- [1] R. R. Søndergaard, M. Hösel, F. C. Krebs, *J. Polym. Sci., Part B: Polym. Phys.* **2013**, *51*, 16.
- [2] T. Leijtens, S. D. Stranks, G. E. Eperon, R. Lindblad, E. M. J. Johansson, I. J. McPherson, H. Rensmo, J. M. Ball, M. M. Lee, H. J. Snaith, *ACS Nano* **2014**, *8*, 7147.
- [3] L. Lu, T. Zheng, Q. Wu, A. M. Schneider, D. Zhao, L. Yu, *Chem. Rev.* **2015**, *115*, 12666.
- [4] H. Sirringhaus, P. J. Brown, R. H. Friend, M. M. Nielsen, K. Bechgaard, B. M. W. Langeveld-Voss, A. J. H. Spiering, R. A. J. Janssen, E. W. Meijer, P. Herwig, D. M. de Leeuw, *Nature* **1999**, *401*, 685.
- [5] J. Mei, Z. Bao, *Chem. Mater.* **2014**, *26*, 604.
- [6] T. S. van der Poll, A. Zhugayevych, E. Chertkov, R. C. Bakus, J. E. Coughlin, S. J. Teat, G. C. Bazan, S. Tretiak, *J. Phys. Chem. Lett.* **2014**, *5*, 2700.
- [7] L. F. Lai, J. A. Love, A. Sharenko, J. E. Coughlin, V. Gupta, S. Tretiak, T.-Q. Nguyen, W.-Y. Wong, G. C. Bazan, *J. Am. Chem. Soc.* **2014**, *136*, 5591.
- [8] Y. Sun, G. C. Welch, W. L. Leong, C. J. Takacs, G. C. Bazan, A. J. Heeger, *Nat. Mater.* **2012**, *11*, 44.
- [9] W. L. Leong, G. C. Welch, L. G. Kaake, C. J. Takacs, Y. Sun, G. C. Bazan, A. J. Heeger, *Chem. Sci.* **2012**, *3*, 2103.
- [10] Z. Li, J. D. A. Lin, H. Phan, A. Sharenko, C. M. Proctor, P. Zalar, Z. Chen, A. Facchetti, T.-Q. Nguyen, *Adv. Funct. Mater.* **2014**, *24*, 6989.
- [11] D. H. Wang, A. K. K. Kyaw, V. Gupta, G. C. Bazan, A. J. Heeger, *Adv. Energy Mater.* **2013**, *3*, 1161.
- [12] N. Yaacobi-Gross, N. D. Treat, P. Pattanasattayavong, H. Faber, A. K. Perumal, N. Stingelin, D. D. C. Bradley, P. N. Stavrinou, M. Heeney, T. D. Anthopoulos, *Adv. Energy Mater.* **2015**, *5*, 1401529.
- [13] A. K. K. Kyaw, D. H. Wang, V. Gupta, W. L. Leong, L. Ke, G. C. Bazan, A. J. Heeger, *ACS Nano* **2013**, *7*, 4569.
- [14] A. Sharenko, C. M. Proctor, T. S. van der Poll, Z. B. Henson, T.-Q. Nguyen, G. C. Bazan, *Adv. Mater.* **2013**, *25*, 4403.
- [15] O. K. Kwon, J.-H. Park, D. W. Kim, S. K. Park, S. Y. Park, *Adv. Mater.* **2015**, *27*, 1951.
- [16] A. Sharenko, N. D. Treat, J. A. Love, M. F. Toney, N. Stingelin, T.-Q. Nguyen, *J. Mater. Chem. A* **2014**, *2*, 15717.
- [17] L. A. Perez, K. W. Chou, J. A. Love, T. S. van der Poll, D.-M. Smilgies, T.-Q. Nguyen, E. J. Kramer, A. Amassian, G. C. Bazan, *Adv. Mater.* **2013**, *25*, 6380.
- [18] A. K. K. Kyaw, D. H. Wang, C. Luo, Y. Cao, T.-Q. Nguyen, G. C. Bazan, A. J. Heeger, *Adv. Energy Mater.* **2014**, *4*, 1301469.
- [19] J. A. Love, C. M. Proctor, J. Liu, C. J. Takacs, A. Sharenko, T. S. van der Poll, A. J. Heeger, G. C. Bazan, T.-Q. Nguyen, *Adv. Funct. Mater.* **2013**, *23*, 5019.
- [20] C. McDowell, M. Abdelsamie, K. Zhao, D.-M. Smilgies, G. C. Bazan, A. Amassian, *Adv. Energy Mater.* **2015**, *5*, 1501121.
- [21] Y. Huang, W. Wen, S. Mukherjee, H. Ade, E. J. Kramer, G. C. Bazan, *Adv. Mater.* **2014**, *26*, 4168.
- [22] I. McCulloch, M. Heeney, M. L. Chabinyc, D. DeLongchamp, R. J. Kline, M. Cölle, W. Duffy, D. Fischer, D. Gundlach, B. Hamadani, R. Hamilton, L. Richter, A. Salleo, M. Shkunov, D. Sparrowe, S. Tierney, W. Zhang, *Adv. Mater.* **2009**, *21*, 1091.

- [23] T. Lei, Y. Cao, Y. Fan, C.-J. Liu, S.-C. Yuan, J. Pei, *J. Am. Chem. Soc.* **2011**, *133*, 6099.
- [24] X. Zhan, A. Faccetti, S. Barlow, T. J. Marks, M. A. Ratner, M. R. Wasielewski, S. R. Marder, *Adv. Mater.* **2011**, *23*, 268.
- [25] D. I. James, S. Wang, W. Ma, S. Hedström, X. Meng, P. Persson, S. Fabiano, X. Crispin, M. R. Andersson, M. Berggren, E. Wang, *Adv. Electron. Mater.* **2016**, *2*, 1500313.
- [26] M. He, W. Li, Y. Gao, H. Tian, J. Zhang, H. Tong, D. Yan, Y. Geng, F. Wang, *Macromolecules* **2016**, *49*, 825.
- [27] A. Zhugayevych, S. Tretiak, *Annu. Rev. Phys. Chem.* **2015**, *66*, 305.
- [28] H. Yu, Z. Bao, J. H. Oh, *Adv. Funct. Mater.* **2013**, *23*, 629.
- [29] H. Yu, Z. Bao, J. H. Oh, *Adv. Funct. Mater.* **2013**, *23*, 525.
- [30] X. Wang, W. Song, B. Liu, G. Chen, D. Chen, C. Zhou, G. Shen, *Adv. Funct. Mater.* **2013**, *23*, 1202.
- [31] H. Wang, W. Deng, L. Huang, X. Zhang, J. Jie, *ACS Appl. Mater. Interfaces* **2016**, *8*, 7912.
- [32] A. K. Palai, J. Lee, S. Das, J. Lee, H. Cho, S.-U. Park, S. Pyo, *Org. Electron.* **2012**, *13*, 2553.
- [33] J. Huang, J. Du, Z. Cevher, Y. Ren, X. Wu, Y. Chu, *Adv. Funct. Mater.* **2017**, *27*, 1604163.
- [34] C. S. Smithson, D. Ljubic, Y. Wu, S. Zhu, *Org. Electron.* **2016**, *37*, 42.
- [35] B. Mukherjee, M. Mukherjee, Y. Choi, S. Pyo, *ACS Appl. Mater. Interfaces* **2010**, *2*, 1614.
- [36] J. H. Jung, M. J. Yoon, J. W. Lim, Y. H. Lee, K. E. Lee, D. H. Kim, J. H. Oh, *Adv. Funct. Mater.* **2017**, *27*, 1604528.
- [37] W. Yao, Y. Yan, L. Xue, C. Zhang, G. Li, Q. Zheng, Y. S. Zhao, H. Jiang, J. Yao, *Angew. Chem., Int. Ed.* **2013**, *125*, 8875.
- [38] G. R. A. M. J. Frisch, G. W. Trucks, H. B. Schlegel, G. E. Scuseria, M. A. Robb, J. R. Cheeseman, G. Scalmani, V. Barone, B. Mennucci, G. A. Petersson, H. Nakatsuji, M. Caricato, X. Li, H. P. Hratchian, A. F. Izmaylov, J. Bloino, G. Zheng, J. L. Sonnenberg, M. Hada, M. Ehara, K. Toyota, R. Fukuda, J. Hasegawa, M. Ishida, T. Nakajima, Y. Honda, O. Kitao, H. Nakai, T. Vreven, J. A. Montgomery Jr., J. E. Peralta, F. Ogliaro, M. Bearpark, J. J. Heyd, E. Brothers, K. N. Kudin, V. N. Staroverov, R. Kobayashi, J. Normand, K. Raghavachari, A. Rendell, J. C. Burant, S. S. Iyengar, J. Tomasi, M. Cossi, N. Rega, J. M. Millam, M. Klene, J. E. Knox, J. B. Cross, V. Bakken, C. Adamo, J. Jaramillo, R. Gomperts, R. E. Stratmann, O. Yazyev, A. J. Austin, R. Cammi, C. Pomelli, J. W. Ochterski, R. L. Martin, K. Morokuma, V. G. Zakrzewski, G. A. Voth, P. Salvador, J. J. Dannenberg, S. Dapprich, A. D. Daniels, O. Farkas, J. B. Foresman, J. V. Ortiz, J. Cioslowski, D. J. Fox, Gaussian Inc., Wallingford CT, **2009**.
- [39] T. Yanai, D. P. Tew, N. C. Handy, *Chem. Phys. Lett.* **2004**, *393*, 51.
- [40] A. Zhugayevych, O. Postupna, H.-L. Wang, S. Tretiak, *Chem. Phys.* **2016**, *481*, 133.
- [41] M. Cossi, N. Rega, G. Scalmani, V. Barone, *J. Comput. Chem.* **2003**, *24*, 669.
- [42] A. Zhugayevych, O. Postupna, R. C. Bakus li, G. C. Welch, G. C. Bazan, S. Tretiak, *J. Phys. Chem. C* **2013**, *117*, 4920.



Supporting Information

for *Adv. Funct. Mater.*, DOI: 10.1002/adfm.201702073

Single Crystal Microwires of *p*-DTS(FBTTh₂)₂ and Their Use in the Fabrication of Field-Effect Transistors and Photodetectors

Qiuhong Cui, Yuanyuan Hu, Cheng Zhou, Feng Teng, Jianfei Huang, Andriy Zhugayevych,* Sergei Tretiak, Thuc-Quyen Nguyen, and Guillermo C. Bazan**

Supporting Information

Single crystal microwires of *p*-DTS(FBTTh₂)₂ and their use in the fabrication of field-effect transistors and photodetectors

QiuHong Cui*, Yuanyuan Hu, Cheng Zhou, Feng Teng, Jianfei Huang, Andriy
Zhugayevych*, Sergei Tretiak, Thuc-Quyen Nguyen and Guillermo C. Bazan*

This PDF file includes:

S1: Additional experimental data.	P1
S2 Introductory comments	P5
S3 Intramolecular vibronic couplings and UV-Vis spectra	P6
S4 Intermolecular electronic couplings and charge/exciton transport	P9
S5 Intramolecular (conformational) disorder	P12
S6 Intermolecular disorder	P13
S7 Alternative intermolecular packings	P14

S1: Additional experimental data

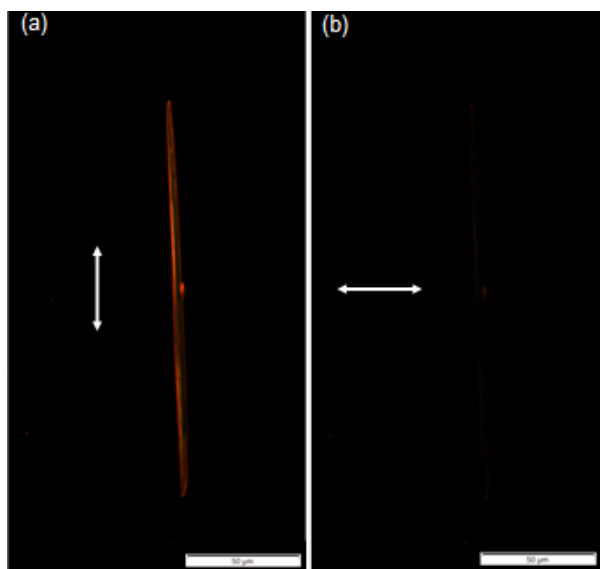


Figure S1: Cross-polarized optical microscopy images of the *p*-DTS(FBTTh₂)₂ microwire. The white arrows indicate the orientation of the crossed polarizers with respect to the wires.

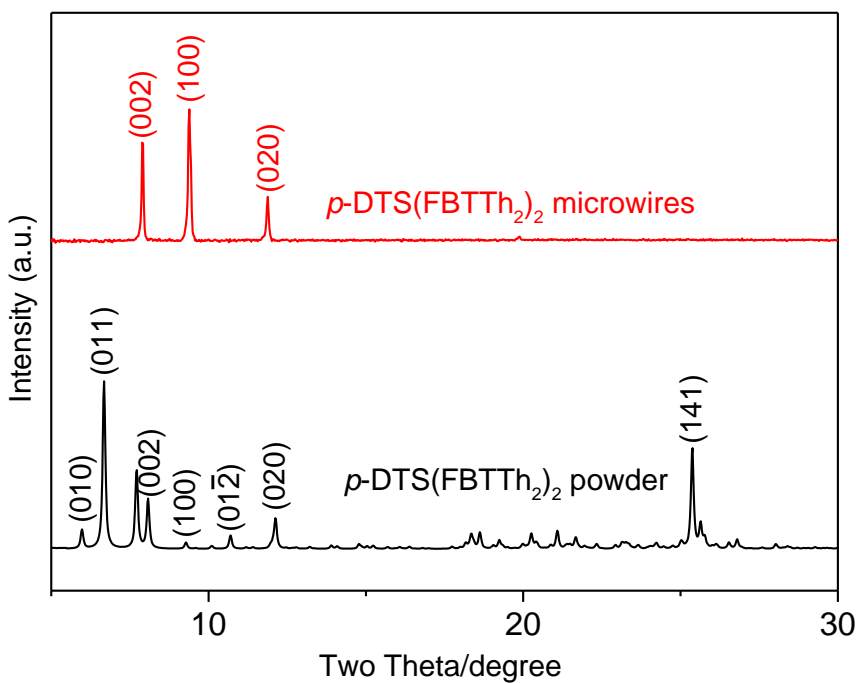


Figure S2: XRD patterns of the *p*-DTS(FBTTh₂)₂ microwires (red) and powder sample (black). The cell parameters of *p*-DTS(FBTTh₂)₂ microwires is $a = 9.2539$ (11) Å, $b = 14.9631(19)$ Å, $c = 22.219(3)$ Å, $\alpha = 81.005^\circ$, $\beta = 85.178^\circ$ and $\gamma = 88.053^\circ$. Combining XRD and SAED observations together, we concluded that microwires grow preferentially along the [100] direction.

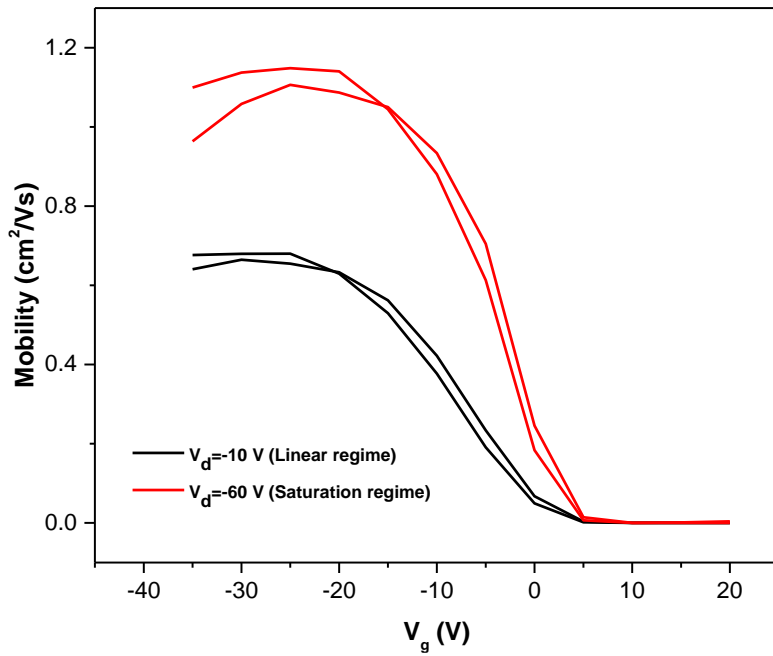


Figure S3: The dependence of mobility on gate voltage for a typical microwire crystal FETs.

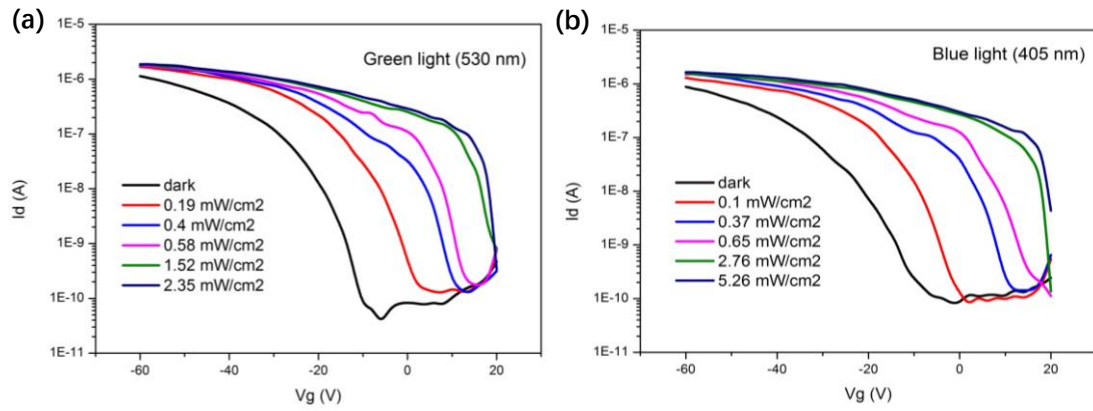


Figure S4: The transfers of the mirowire crystal-base phototransistors under different irradiation intensity: (a) Green light (530 nm) and (b) Blue light (405 nm).

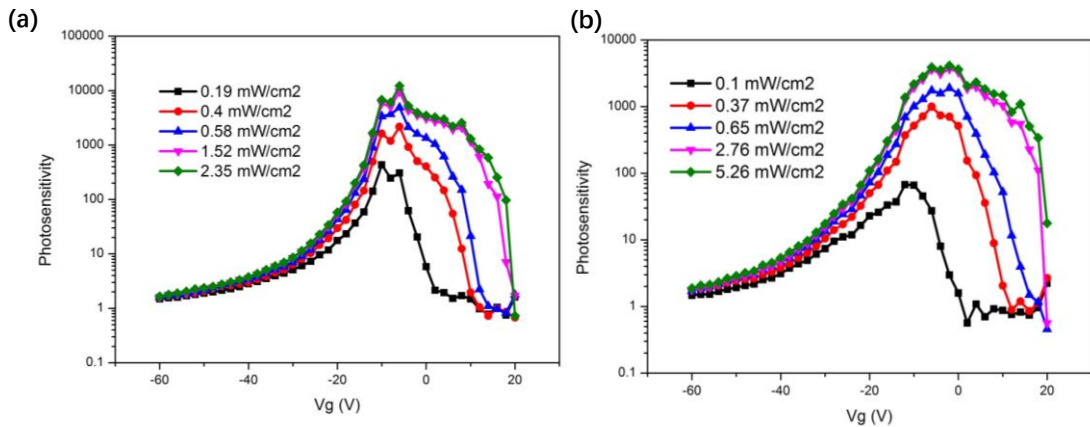


Figure S5: The photosensitivity of the mirowire crystal-base phototransistors under different irradiation intensity: (a) Green light (530 nm) and (b) Blue light (405 nm).

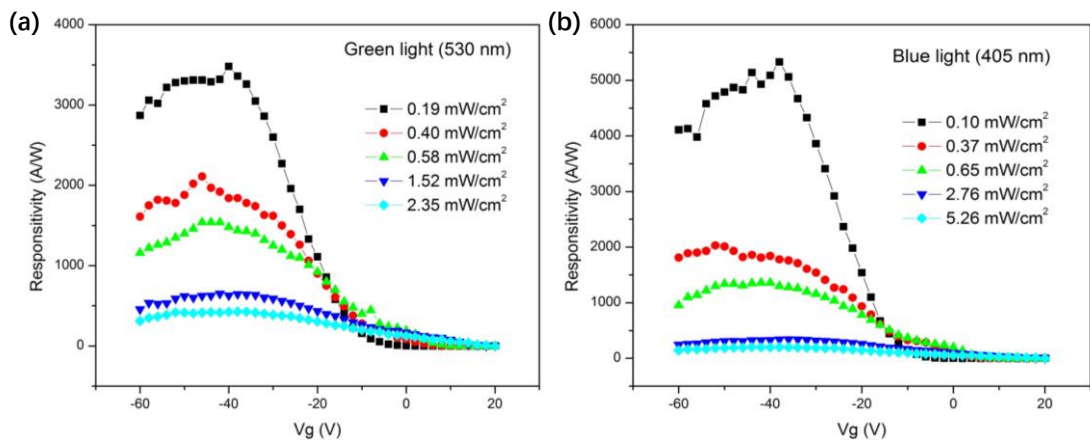


Figure S6: The responsivity of the mirowire crystal-base phototransistors under different irradiation intensity: (a) Green light (530 nm) and (b) Blue light (405 nm).

S2 Introductory comments

Zero-field charge carrier mobility can be represented as follows [1]:

$$\mu_0 \approx f \times (a[\text{\AA}] \cdot t)^2 \times \frac{1}{W(T)^2} \frac{\text{cm}^2}{\text{V} \cdot \text{s}}, \quad (\text{S1})$$

where f is the lattice form-factor, t is the transfer integral, a is the hopping distance, and W is the *spectral overlap bandwidth* given by $\sqrt{T/J(T)}$, where $J(T)$ is the spectral overlap and T is the temperature. The three factors above are nearly independent and thus will be analyzed separately. The first one, lattice form-factor is equal to 1 for π -stacks. The other two are analyzed below.

Rescaling vibronic couplings

Vibrational frequencies ω and corresponding Huang–Rhys factors S_ω are rescaled by the same factor c_ω . The set of factors c_ω satisfies the equation $\sum_\omega c_\omega^2 \lambda_\omega = \lambda_{\text{exact}}$, where $\lambda_\omega = S_\omega \hbar \omega$. Low-frequency modes are usually more anharmonic than high-frequency ones. An ad-hoc solution is to set

$$c_\omega = \sqrt{1 - A \exp\left(-\frac{\hbar^2 \omega^2}{2\sigma^2}\right)}, \text{ where } A = \frac{\sum_\omega \lambda_\omega - \lambda_{\text{exact}}}{\sum_\omega \lambda_\omega \exp\left(-\frac{\hbar^2 \omega^2}{2\sigma^2}\right)} \quad (\text{S2})$$

and σ is a free parameter. In the present work we use $\sigma = 0.2$ eV. The value of λ_{exact} is estimated as

$$2\lambda_{\text{exact}} = E_{10} - E_{00} + E_{01} - E_{11}, \quad (\text{S3})$$

where 00 is the ground state in ground state geometry, 10 is the state of interest in ground state geometry, 01 is the ground state in the state of interest geometry etc.

S3 Intramolecular vibronic couplings and UV-Vis spectra

Table S1: Anharmonic and asymmetry corrections (all in meV) to calculated vibronic couplings. Here λ is the polaron relaxation energy calculated via energy difference and averaged over the two states, $\Delta\lambda = \lambda - \sum_{\hbar\omega} S_\omega \hbar\omega$ where ω is the frequency and S_ω is the Huang–Rhys factor of a given vibrational mode, and $\lambda_0 = \lambda(\text{molecule}) - \lambda(\pi\text{-backbone})$.

	λ	$\Delta\lambda$	λ_0
cation	230	6	12
anion	190	20	22
excited singlet	300	25	30

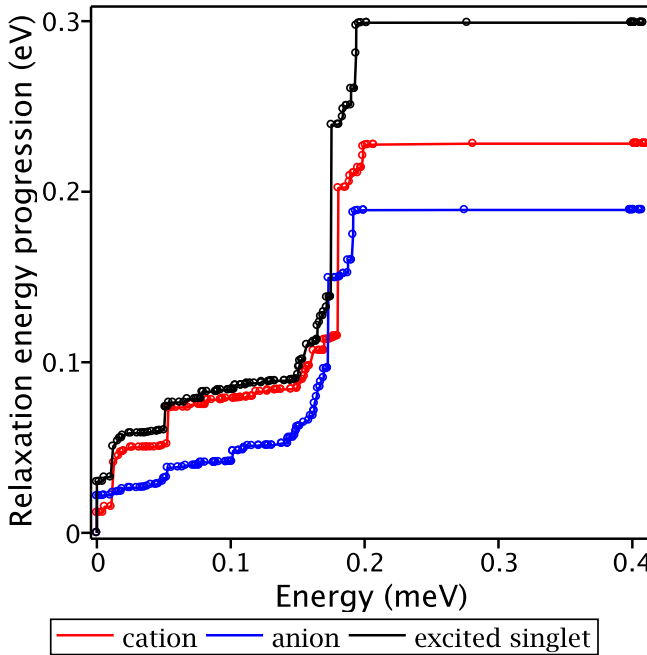


Figure S7: Relaxation energy progression for cation, anion, and the lowest excited singlet in chloroform: $\lambda(E) = \sum_{\hbar\omega < E} S_\omega \hbar\omega$. Because of anharmonicity a number of vibrational modes are considered classically with the total relaxation energy λ_0 listed in Table S1.

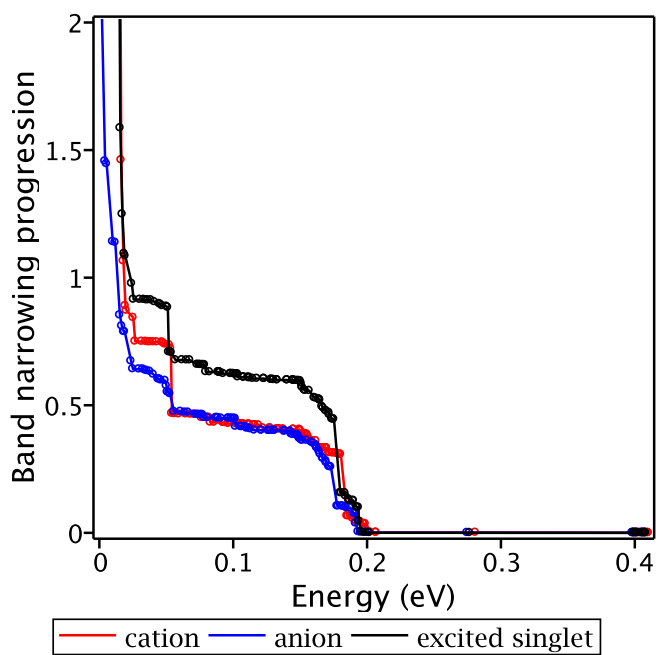


Figure S8: Polaron band narrowing progression (progress from right to left) at 300 K for holes, electrons, and excitons: a value of α means band narrowing factor $e^{-2\alpha}$ for transfer integrals between the two identical molecules. This figure shows that thermally equilibrated vibrations with $\hbar\omega > 50$ meV narrows polaron bands down to tens of meV thus localizing charge carriers and Frenkel excitons.

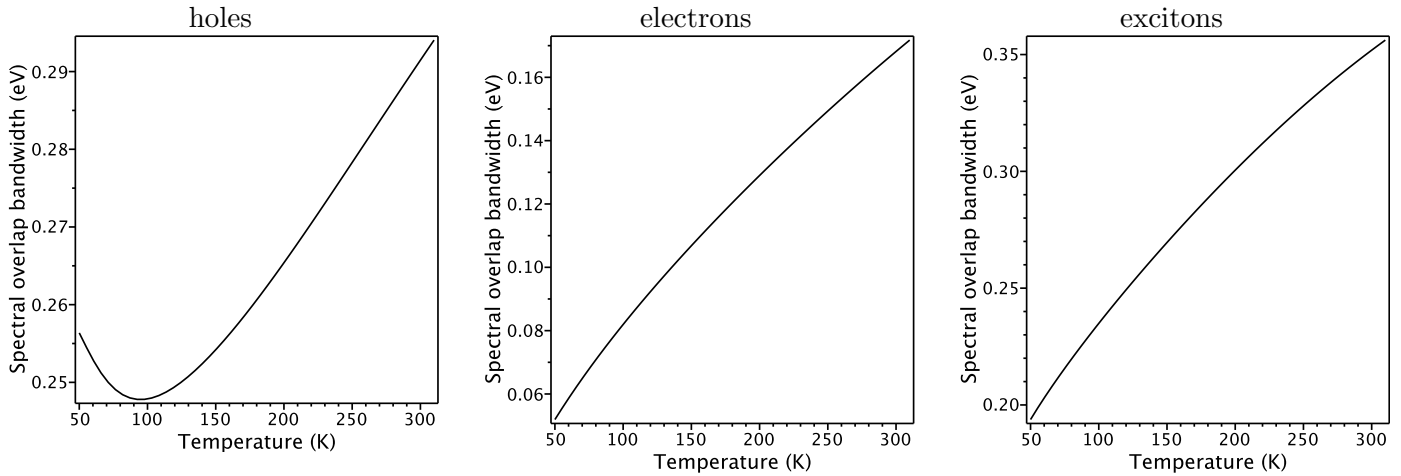


Figure S9: Temperature dependence of the spectral overlap bandwidth for holes, electrons, and excitons. Inhomogeneous broadening is set to zero.

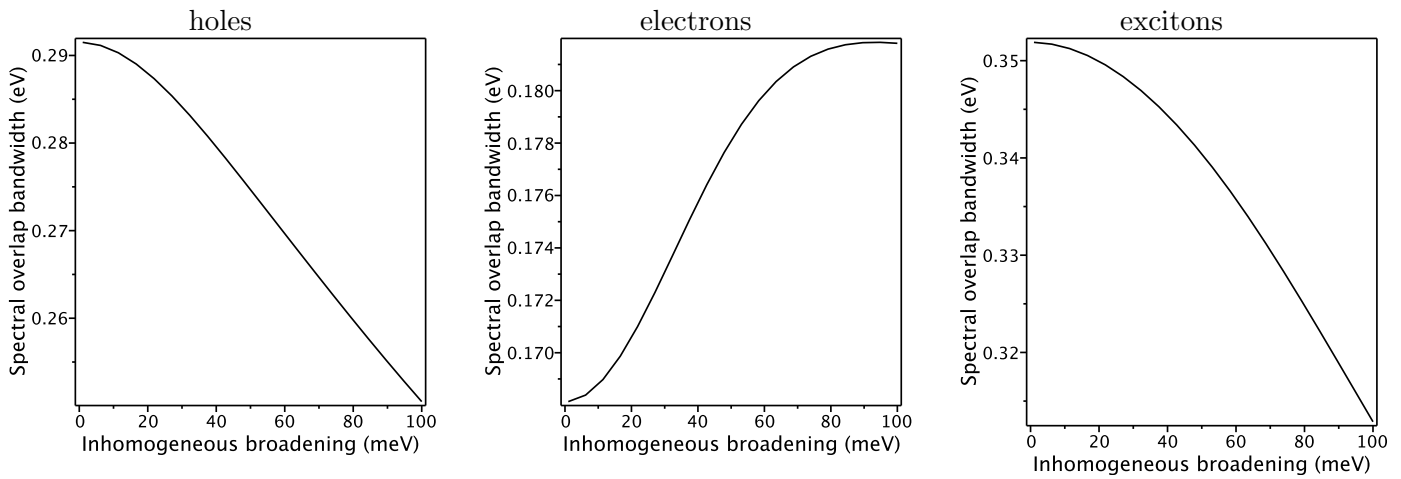


Figure S10: Dependence of the spectral overlap bandwidth at 300 K for holes, electrons, and excitons on inhomogeneous broadening. The dependence saturates at small values because of nonzero intrinsic broadening caused by classical vibrational modes.

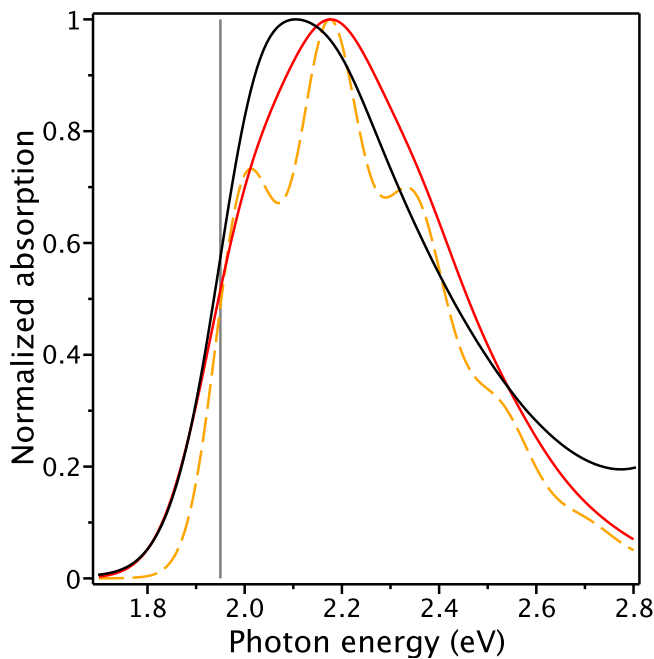


Figure S11: The lowest energy UV-Vis absorption band of the molecule: calculated band (red and orange curves) is superimposed on measured spectrum in solution (black curve) by shifting the former by -0.11 eV. The vertical gray line marks 0-0 transition. The dashed orange curve corresponds to zero line broadening, whereas for the solid red curve Gaussian broadening with $\sigma = 70$ meV is introduced. Note that the calculations are performed for the conformer observed in the crystal.

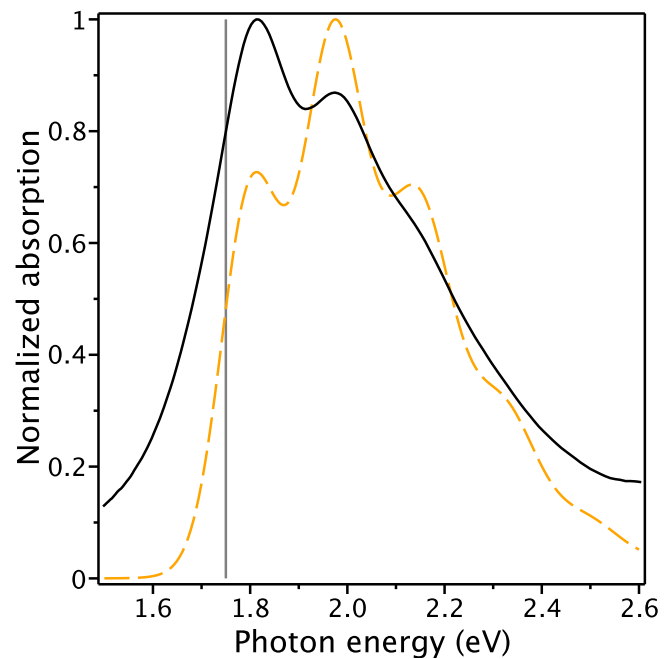


Figure S12: The same calculated band (orange curve) is superimposed on measured spectrum of annealed film (black curve) by shifting the former by -0.3 eV to match the position of the three visible peaks.

S4 Intermolecular electronic couplings and charge/exciton transport

Table S2: Transfer integrals (intermolecular couplings) and efficiencies for holes, electrons, and Frenkel excitons. Here the monomer code ‘ $m\ ijk$ ’ means molecule number m translated by i unit cells along the first translation vector, by j along the second translation vector, and by k along the third vector. The coupling is given between the monomer ‘1 000’ and the listed monomer. Only symmetry nonequivalent dimers are listed, their multiplicity per unit cell is given in ‘mul’ column. The distance a is the center-to-center (hopping) distance. The transfer efficiency is the product t^2a^2 given in eV $^2\text{\AA}^2$ and is proportional to the contribution of the given transfer to the charge carrier mobility along the direction of the transfer [1].

monomer	mul	$t(\text{meV})$	$a(\text{\AA})$	eff
Holes				
1 100	4	104	9	.919
1 3̄10	4	-4	31	.014
2 3̄10	2	-1	16	.000
Electrons				
1 100	4	15	9	.020
2 4̄10	2	6	23	.016
2 000	2	4	23	.007
2 1̄00	2	4	16	.004
2 3̄10	2	4	16	.004
1 3̄10	4	1	31	.000
Excitons				
1 3̄10	4	-14	31	.179
2 4̄10	2	16	23	.133
2 5̄10	2	11	31	.105
2 2̄10	2	-21	14	.081
1 100	4	30	9	.080
2 100	2	8	31	.067
2 2̄00	2	-19	14	.064
1 2̄10	4	-10	23	.054
2 000	2	10	23	.054
1 4̄10	4	-6	39	.049
2 3̄00	2	-12	17	.042
2 6̄10	2	5	39	.033
2 1̄10	2	-10	17	.027
1 300	4	-6	28	.027
2 5̄20	2	4	37	.024
2 3̄10	2	-9	16	.023
2 200	2	4	39	.022
1 010	4	10	15	.021
2 6̄20	2	3	44	.020

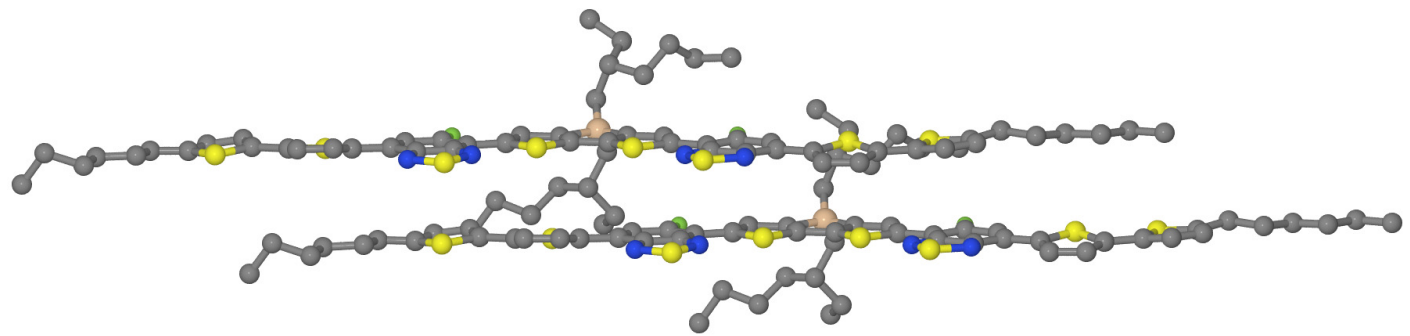


Figure S13: Dimer 1 000 + 1 100.

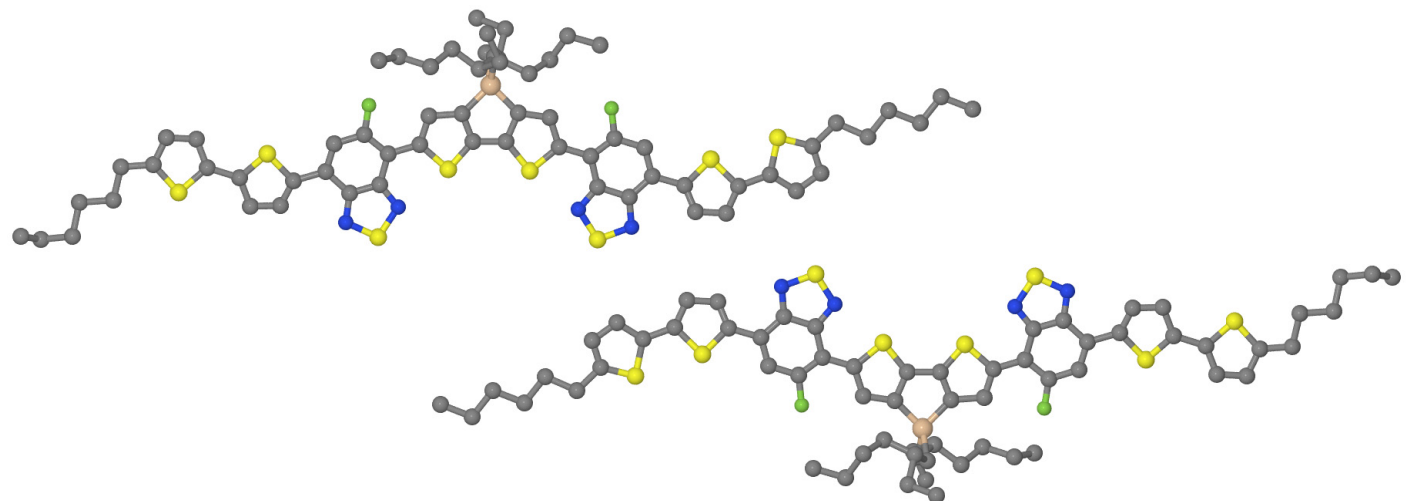


Figure S14: Dimer 1 000 + 2 410.

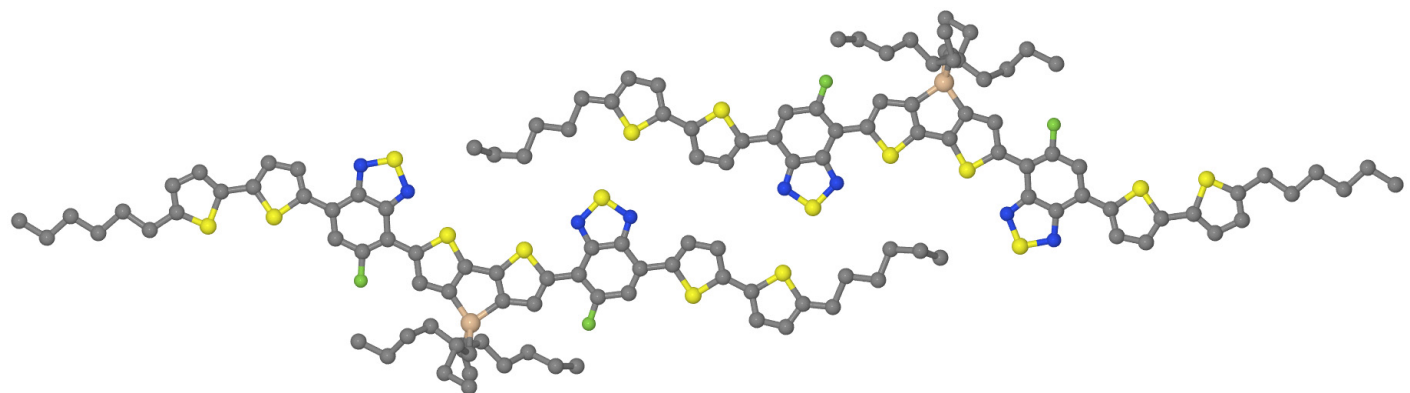


Figure S15: Dimer 1 000 + 2 000.

Zero-field mobility tensor for holes corresponding to the spectral overlap bandwidth $W = 292$ meV (at 300 K with zero inhomogeneous broadening):

$$\begin{pmatrix} 10. & -0.07 & 0.0002 \\ -0.07 & 0.04 & -0.0002 \\ 0.0002 & -0.0002 & 0.0003 \end{pmatrix} \frac{\text{cm}^2}{\text{V} \cdot \text{s}} \quad (\text{S4})$$

The same for electrons ($W = 168$ meV):

$$\begin{pmatrix} 1.0 & -0.14 & 0. \\ -0.14 & 0.07 & 0. \\ 0. & 0. & 0.00001 \end{pmatrix} \frac{\text{cm}^2}{\text{V} \cdot \text{s}} \quad (\text{S5})$$

The same for excitons under hypothetical assumption of infinite lifetime ($W = 352$ meV):

$$\begin{pmatrix} 5.2 & -1.5 & -0.02 \\ -1.5 & 1.9 & 0.01 \\ -0.02 & 0.01 & 1.1 \end{pmatrix} \frac{\text{cm}^2}{\text{V} \cdot \text{s}} \quad (\text{S6})$$

Averaged diffusion length for excitons (radiative lifetime is 1.8 ns) is 100 nm.

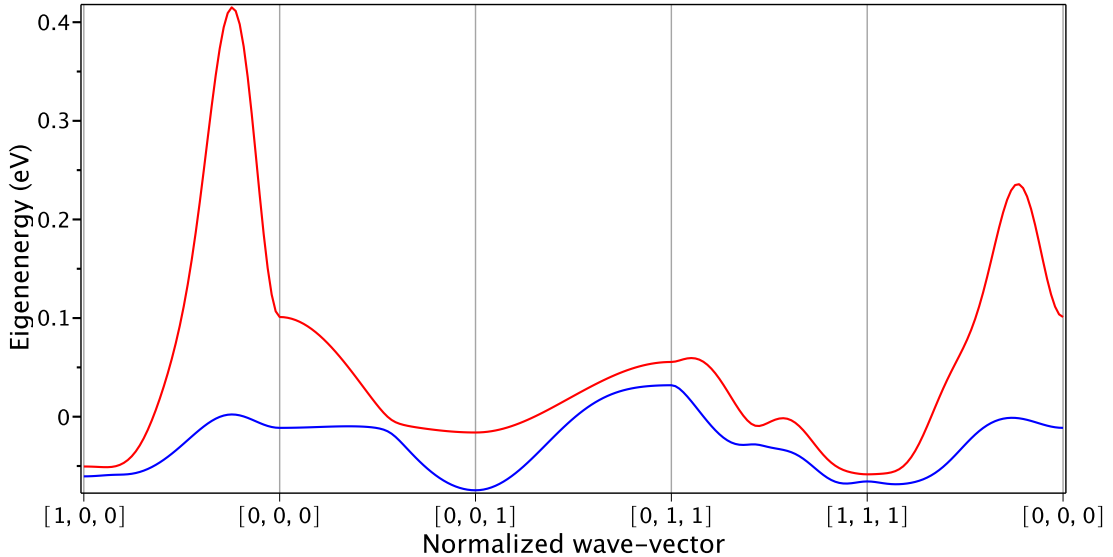


Figure S16: Bare exciton bands (without band narrowing).

S5 Intramolecular (conformational) disorder

Table S3: Relative energies of different rotamers: E_1 is the energy cost for flipping the terminal thiophene, E_2 is for flipping the dihedral between thiophene and benzene ring, E_3 is for flipping one of the two central dihedrals, E_{33} is for flipping both of them, and E_{133} is the relative energy of the conformer observed in the crystal. Calculations made by CAM-B3LYP/6-31G* are from Ref. [2] to be compared with a priori more accurate CAM-B3LYP-D3/6-311G* [3] calculations made in the present work.

method	solvent	E_1	E_2	E_3	E_{33}	E_{133}
CAM-B3LYP/6-31G*	vacuum	31	30	24	46	75
CAM-B3LYP/6-31G*	chloroform	27	6	17	33	59
CAM-B3LYP-D3/6-311G*	vacuum	27	24	12	20	46
CAM-B3LYP-D3/6-311G*	chloroform	24	6	7	11	35

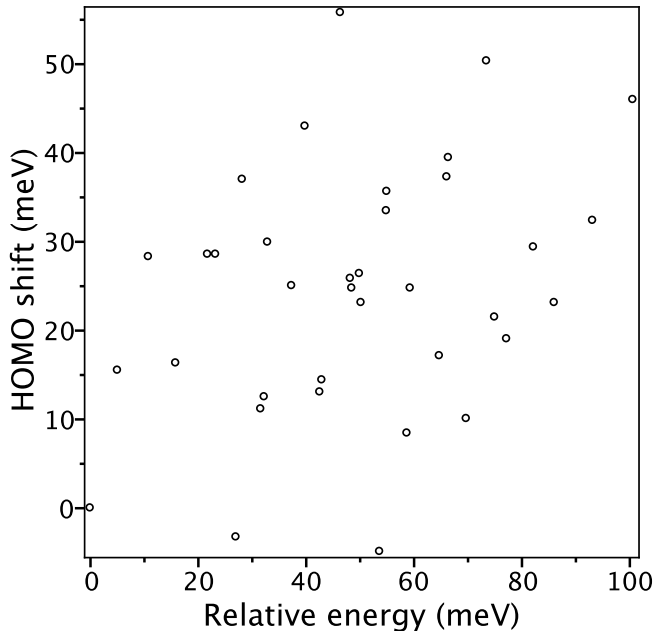


Figure S17: HOMO energy shift for all possible rotamers. Being partitioned into contribution of rotation of individual dihedrals, the shift is -3 meV for terminal dihedrals, and $+15$ meV for other dihedrals.

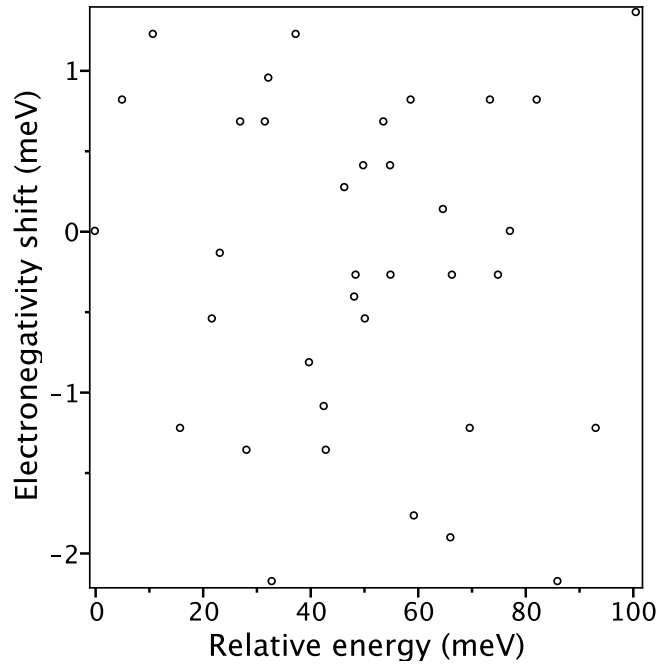


Figure S18: Electronegativity (middle of the gap) shift for all possible rotamers. Small values imply that HOMO and LUMO shifts are nearly antisymmetric.

S6 Intermolecular disorder

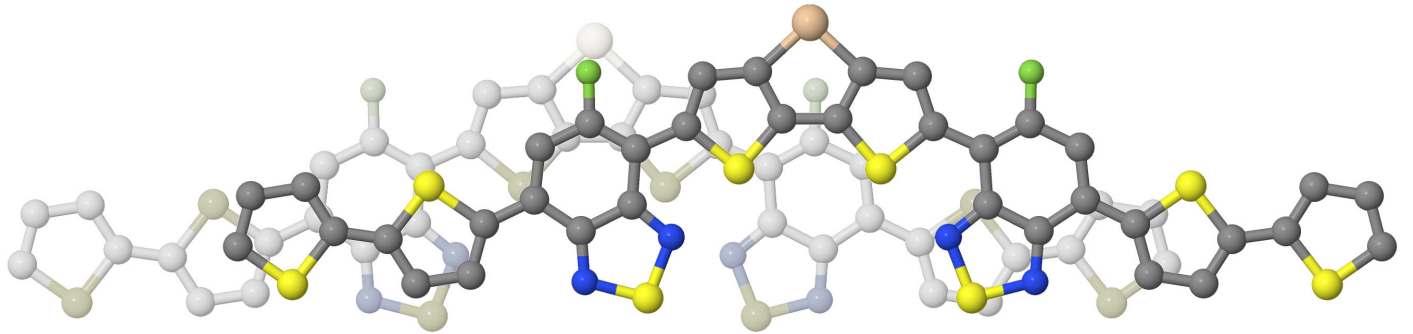


Figure S19: Dimer: top-view.

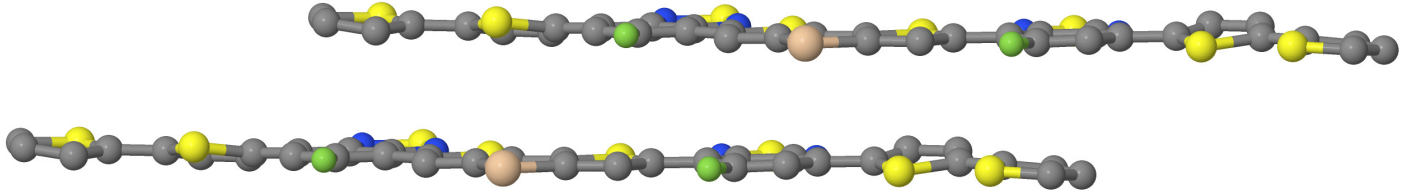


Figure S20: Dimer: side-view.

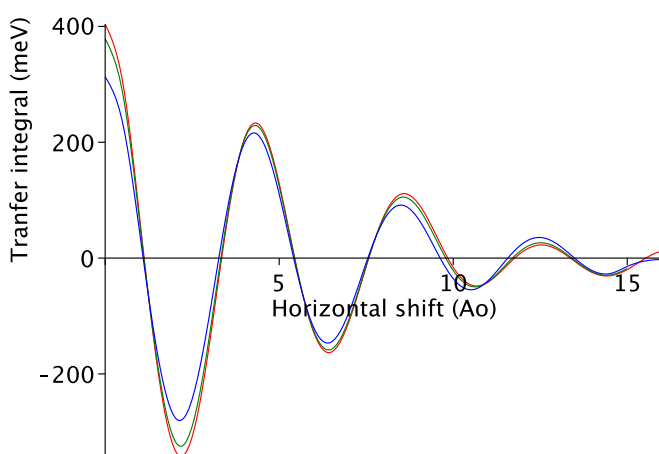


Figure S21: Oscillations of intermolecular couplings for holes with relative in-plane shifts of the two monomers in the dimer. The horizontal axis corresponds to left-right shift in Fig. S19, whereas different colors mark up-down shifts in Fig. S19 (π - π separation is fixed at 3.43 Å). Couplings are calculated by PM6 semimempirical method and then rescaled by a factor of 4 to match ZINDO and CAM-B3LYP/6-31G* values at limited set of points.

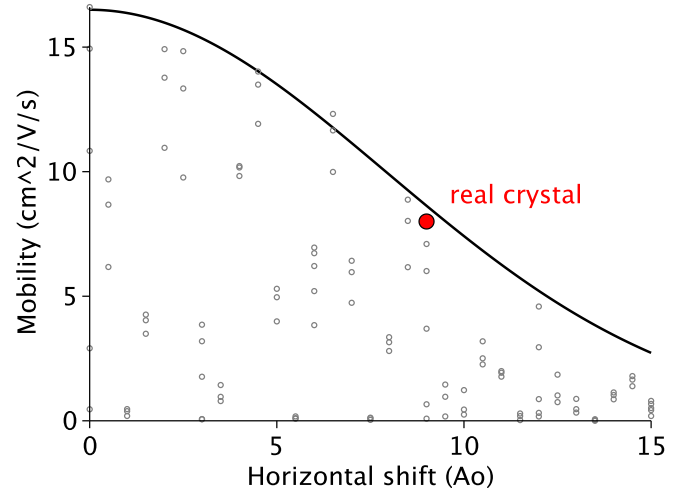


Figure S22: Dependence of the mobility on the mutual positon of molecules in the π -stack calculated at 300 K from Fig. S21 within the small polaron hopping approximation [1]. The vibronic couplings entering the spectral overlap [1] are estimated at CAM-B3LYP/6-31G* level of theory. The experimentally observed geometry of the π -stack is marked by red circle. Black dots represent all scanned geometries.

S7 Alternative intermolecular packings

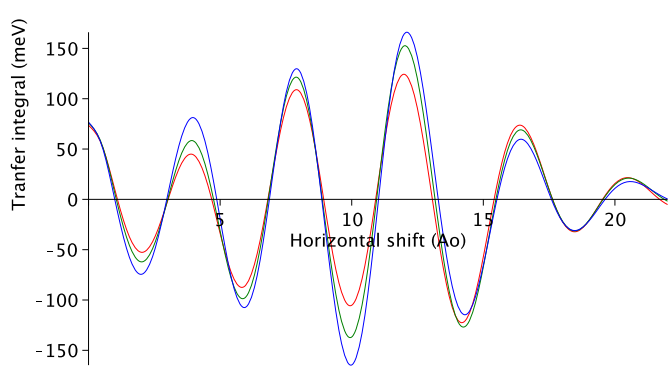


Figure S23: The same as Fig. S21 but with antiparallel packing relevant for the alternative polymorph discussed in Ref. [2].

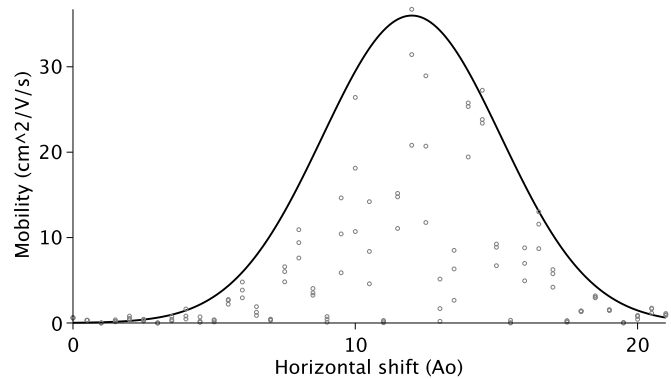


Figure S24: The same as Fig. S22 but with antiparallel packing.

References

- [1] A Zhugayevych, S Tretiak, Theoretical Description of Structural and Electronic Properties of Organic Photovoltaic Materials, *Annu Rev Phys Chem* 66, 305 (2015)
- [2] T S van der Poll, A Zhugayevych, E Chertkov, R C Bakus II, J Coughlin, G C Bazan, S Tretiak, Polymorphism of Crystalline Molecular Donors for Solution-Processed Organic Photovoltaics, *J Phys Chem Let* 5, 2700 (2014)
- [3] S Grimme, S Ehrlich, L Goerigk, Effect of the damping function in dispersion corrected density functional theory, *J Comp Chem* 32, 1456 (2011)